Applied Surface Science Advances 6 (2021) 100144

Contents lists available at ScienceDirect

Applied Surface Science Advances

journal homepage: www.sciencedirect.com/journal/applied-surface-science-advances

Inkjet printed $CuIn_{(1-X)}Ga_XSe_2$ thin film by controlled selenium distribution for improved power conversion efficiency in chalcopyrite solar cells

Brijesh Singh Yadav [a,b], Suhash Ranjan Dey [b], Sanjay R. Dhage [a,*]

[a] Centre for Solar Energy Materials, International Advanced Research Center for Powder Metallurgy and New Materials (ARCI), PO Balapur, Hyderabad 50005, India
[b] Materials Science and Metallurgical Engineering Department, Indian Institute of Technology Hyderabad, Kandi, Sangareddy 502285, India

ARTICLE INFO

Keywords:
CIGS
Inkjet printing
Se vapor
Graphite box geometry
Fine-grained layer

ABSTRACT

Selenium (Se) vapor pressure is a key factor during the selenization of $CuIn_{1-X}Ga_X$ (CIG) film to obtain a high-quality $CuIn_{1-X}Ga_XSe_2$ (CIGS) absorber layer. To investigate the effect of Se vapor distribution on the grain growth of inkjet printed precursor film, two geometries of graphite box (square and circular) are used. The results revealed that selenization in the round graphite box give rise to uniform surface coverage and suppressed fine-grained layer due to adequate and uniform distribution of Se vapor. In contrast, film selenized in a square graphite box exhibits high strain and low crystallinity with a thick fine-grained layer. Probable Se vapor distribution inside the graphite box based on internal geometrical constraint and its impact on crystal phase and microstructure is discussed. Finally, CIGS devices fabricated using films selenized in a round graphite box demonstrates higher power-conversion efficiency of 5.2%, owing to high light absorption and efficient carrier separation. Based on J-V and EQE results, probable losses and recombination in the devices are examined and discussed.

1. Introduction

Chalcopyrite Cu(In, Ga)Se_2(CIGS) absorber material emerged as a leading candidate among thin film technologies with a record solar cell efficiency of 23.35% on lab scale and 17% on module scale [1,2]. Non-vacuum processing of CIGS thin film solar cells turns out to be a potential alternative to vacuum-based techniques because of its benefits such as low fabrication cost, rapid deposition and scalability. The best device fabricated by the non-vacuum method showed a champion efficiency of 17.3%, employing a hydrazine solvent, which is toxic and explosive [3,4]. In the search for a benign approach, various non-hydrazine-based routes have been developed and explored. In 2016, Xin et al. reported an 11.3% efficient CIGSSe device by inkjet printing using isopropyl alcohol (IPA) as solvent [5]. Park et al. deposited precursor film by spin coating using methanol as solvent, and the fabricated device demonstrated 14.4% efficiency [6]. However, the additional requirement of multiple selenization steps using toxic gases (H_2S/H_2Se) as a selenium source makes these routes risky, slow, and unfavorable for large area deposition.

In this regard, Se vapor (i.e., vaporization of Se pellets) have been used as a Se source for selenization of precursor film [7–10]. Despite the simplicity and non-toxic advantage, the CIGS film selenized in the presence of Se vapor, the grain growth is not adequate and leads to the bi-layered structure, upper big-grained layer (CIGS-L) and small-grained bottom layer (CIGS-F) [11–13]. This phenomenon is more frequently to arise in CIGS prepared by the sequential deposition of the precursor layer and post-selenization caused by the in-homogenous distribution of precursor elements and the lack of Se vapor [14,15]. One of the common methods is doping alkali elements such as Na into CIGS films [15,16] to improve the absorber film's crystallinity. The role of dopants involves the formation of fluxing agents, which helps facilitate CIGS grain growth. Inappropriately, doping methods increase the fabrication process's complexity, and it is hard to eliminate the existence of CIGS-F.

Additionally, multiple annealing steps in a different atmosphere (Se/N_2/Se) for a longer selenization time can promote the inter-diffusion of elements and improve the grain growth of CIGS [16]. The long duration of the selenization process will induce substantial $MoSe_2$ formation, which degrades the final device performance significantly. Excess Se content in the graphite box was also used earlier to obtain single-layered CIGS film [17,18]. Nevertheless, the inevitable formation of rod-like morphology on the film surface because of excess Se vapor condensation degrades cell performance. Moreover, the removal of deposited Se

* Corresponding author.
E-mail address: dhage@arci.res.in (S.R. Dhage).

https://doi.org/10.1016/j.apsadv.2021.100144
Received 16 March 2021; Received in revised form 28 June 2021; Accepted 12 August 2021
Available online 24 August 2021

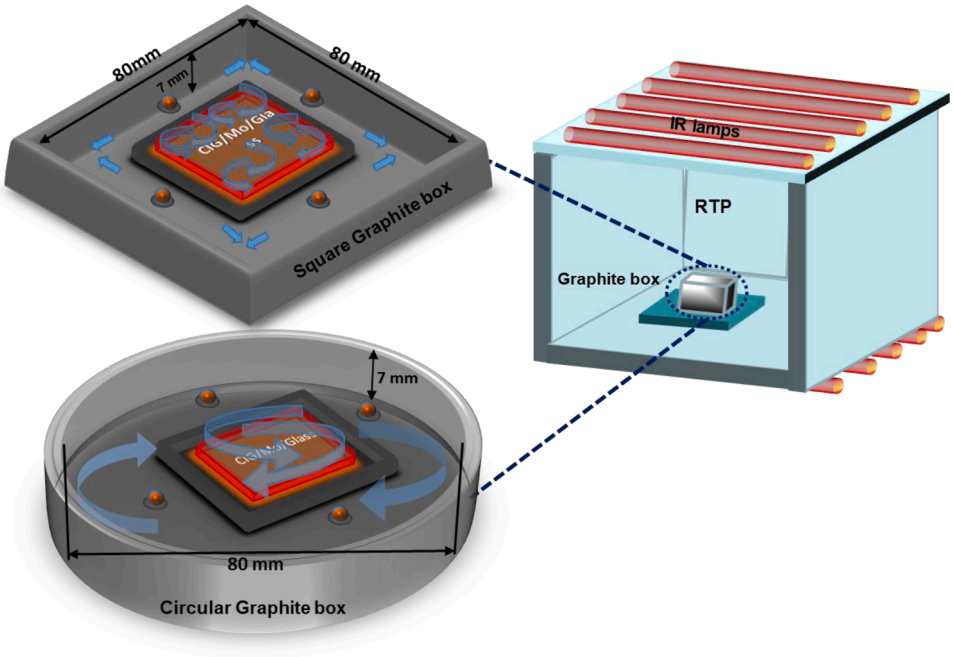

Fig. 1. Schematic of selenization setup with two different types of graphite box geometry, square and circular, used in the process.

on the selenization chamber's wall is highly challenging and time-consuming. Therefore, it is of great interest to obtain large-grained CIGS with the appropriate composition using a simple and low-cost method. Different research groups have utilized the various graphite box to improve the Se vapor distribution to enhance CIGS grain growth and reduce the CIGS-F layer [19]. Han et al. study the influence of partial pressure of Se vapor (P_{Se}) generated inside the closed graphite box for solution-processed CIGS solar cells [20]. They revealed that P_{Se} is mainly controlled by the graphite box chamber's background pressure and affects the Cu–Se liquid formation at the initial stages of film growth responsible for the morphological difference. Ulicna et al. implied the closed graphite box with a partial opening in the lid that resulted in a Se compositional gradient along with the CIGS depth and decrease device performance [21]. Later, Zhao et al. employed the graphite box with a pinhole-free lid to increase Se vapor intensity and obtained large-grained CIGS film without CIGS-F layer and demonstrated device efficiency of 11.8% [22]. It is evident that a closed graphite box significantly influences the Se vapor distribution, eventually, the CIGS film's quality.

To the best of our knowledge, no reports are there on the effect of graphite box geometry on grain growth of the CIGS absorber layer. Apart from that, the graphite box's geometry in terms of clearance volume (a gap between the substrate surface and the lid) and shape can have a notable impact on the intensity and distribution of Se vapor according to the model developed by J.J.Scragg et al. for CZTS thin film solar cell [23]. In this respect, we have examined and compared the impact of Se vapor distribution using two different graphite boxes (square & circular) on the structural, morphological, and electrical properties of the inkjet printed precursor film, consequent impact on the performance of CIGS solar cells. Improved graphite box geometry resulted in high crystallinity, uniform grain growth, and the suppression of the CIGS-F layer, which eventually resulted in improved power-conversion efficiency of 5.2%.

2. Material and methods

The precursor film (i.e., CIG) was deposited on sputtered Mo coated soda-lime glass substrate by inkjet printing. Bi-layered Mo thin film (seed + bulk) of about 800 nm was prepared by DC magnetron sputtering (VISTARIS 600, Singulus Technology AG) on SLG substrate used as a bottom electrode; the process parameters were elaborated in our earlier work [24,25]. The CIG precursor ink was formulated by dissolving the individual Cu, In, and Ga nitrate hydrate precursors in a polyethene glycol (PEG) solution and deionized water. To achieve copper poor stoichiometry in final CIGS, the Cu/Ga+In (CGI) and Ga/Ga+In (GGI) ratios in ink were taken as 0.99 and 0.27, respectively, for all the experiments presented in this work. The inkjet printing (L-Series Inkjet printer, Ceradorp, France) and pre-annealing of the precursor layer were repeated five times to achieve the desired film thickness. The ink formulation and printing strategy were adapted from our earlier published work [26,27]. Inkjet printed films were selenized in the RTP furnace (QualiflowTherm, France) using a square graphite box (hereafter referred to as SB) and circular graphite box (hereafter referred to as CB) as presented schematically in Fig. 1. The internal volume of the SB and CB is calculated as 44.8 cm^3 and 35.16 cm^3, respectively. Se pellets (four Se pellets each of about 50 mg) were used as a selenium source, and the selenization process was performed under a continuous flow of N_2 gas.

In this study, two-step selenization profiles are used; 250°C with a holding time of 10 min and 550°C with 14 min. Based on earlier reported literature, it is anticipated that the two-step selenization process would generate adequate P_{Se}, promote proper mixing of precursors and transform CIG into CIGS. It is well reported that the selenization of the CIG precursor begins at about 480°C to form a CIGS phase. Yet, a higher temperature of about 550°C is required to moderate secondary phases and achieve grain growth in CIGS [28,29]. The CIGS phase formation during the selenization of the CIG precursor was intensively investigated in the past [30]. Given this and based on earlier reports, a selenization temperature of 550°C was selected. The selenization time of 14 min has already been optimized to obtain a highly crystalline chalcopyrite phase of the CIGS absorber from the inkjet printed CIG precursor film was taken from our previous paper [31]. Subsequently, 60 nm CdS film was deposited on top of the prepared CIGS absorber layer using a well-proven chemical bath deposition to form a p-n junction [32]. The window layers consisting of i-ZnO (50 nm)/Al: ZnO (900 nm) was sputtered (VISTARIS 600, Singulus Technology AG) on the CdS/CIGS/Mo/Glass stacks; deposition parameters are discussed in our earlier publication [33]. The silver paste point contact was used on the

Table 1
XRF elemental composition data of CIGS absorber films selenized using two different approaches; SB and CB.

Sample ID	Thickness(nm)	Cu%	In%	Ga%	Se%	CIG	GIG	SCIG
SB1	1.28 ± 0.18	22.60 ± 0.22	14.44 ± 0.53	5.20 ± 0.79	57.96 ± 2.38	1.15	0.26	1.37
SB2	1.31 ± 0.09	21.23 ± 0.93	15.56 ± 0.77	5.05 ±0.85	58.16 ± 1.14	1.03	0.25	1.39
SB3	1.29 ± 0.12	20.01 ± 0.71	14.63 ± 1.19	4.79 ± 0.97	60.57 ± 1.23	1.03	0.24	1.54
SB4	1.30 ± 0.07	21.72 ± 0.69	15.82 ± 0.95	5.48 ± 0.59	53.50 ± 2.69	1.01	0.25	1.24
CB1	1.34 ± 0.04	21.84 ± 0.33	16.35 ± 0.56	4.83 ± 0.48	56.98 ± 0.89	1.02	0.23	1.32
CB2	1.32 ±0.03	21.22 ± 0.40	16.01 ± 0.86	4.80 ± 0.36	57.96 ± 0.43	1.02	0.24	1.37
CB3	1.34 ± 0.01	21.15 ± 0.19	16.76 ± 0.25	4.19 ± 0.53	57.90 ± 0.37	1.01	0.25	1.37
CB4	1.35 ± 0.06	22.14 ± 0.02	16.50 ± 0.28	5.21 ± 0.56	56.15 ± 0.25	1.02	0.24	1.28

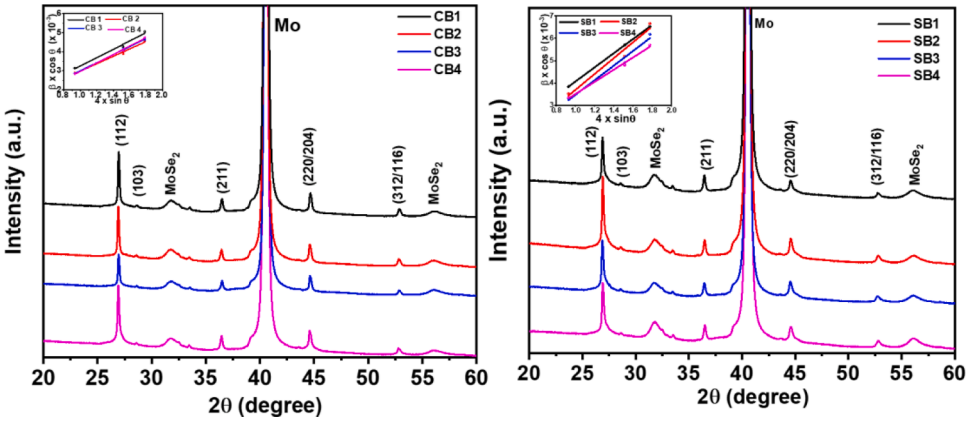

Fig. 2. XRD pattern of CIGS absorber films prepared using two different graphite boxes SB and CB. The corresponding plots of $\beta \cos\theta$ versus 4 * $\sin\theta$ are attached in the inset of respective XRD pattern.

top of the isolated active cell area of 0.18 cm^2 scribed by mechanical scribing for current-voltage (J-V) measurements. All the devices presented in this work are without any anti-reflective coating.

Structural analysis of the CIGS films is determined by XRD (CuKα radiation, D8 Advance, Bruker, Germany). The film compositions are measured by XRF (Model: XDV-SDD, Make: Helmut Fischer, Switzerland) technique. The surface and cross-sectional morphologies of the CIGS films are examined by FESEM (ZEISS, Gemini-500). The topography of CIGS film is studied using a stylus profilometer (DektakXT, Bruker) on a 10 mm × 10 mm scanning area with a 50 nm stylus radius. The device performance of the CIGS solar cells is evaluated by Newport Oriel solar simulator equipped with a Xenon lamp and Keithley source meter under the standard AM1.5G condition. The external quantum efficiency (EQE) was measured by a Bentham PVE 300 system in the wavelength range of 300 nm to 1200 nm.

3. Results and discussion

SB and CB graphite boxes were used to selenize the inkjet printed CIG precursor film, as shown in Fig. 1. The elemental composition at different segments of selenized CIGS film denoted as SB1, SB2, SB3, SB4, CB1, CB2, CB3 and CB4 (refer Fig. 3) is determined by XRF and summarized in Table 1. It is evident that all the selenized films are slightly copper-rich (Cu/Ga+In >1) owing to the evaporation of individual metal selenide during selenization, in good agreement with the earlier literature [34]. Also, minor variation in Cu/Ga+In (CGI) and Ga/Ga+In (GIG) ratios is observed in the case of SB sample segments, whereas no significant change is detected in CB sample segments. The Se/(Cu+In+Ga) (SCIG) ratio, which accounts for the stoichiometric formation of CIGS films, is more than 1 in both cases implying the absorption of Se in the Mo film to form $MoSe_2$. The noticeable disparity in SCIG ratio was found in SB segments (From SB1 to SB4), presumably due to the off-stoichiometry reaction of precursor film with the Se vapor. This phenomenon of non-uniform selenization can be related to the non-uniform Se vapor distribution during selenization.

Table 2
A summary of crystallite size and strain determined using W-H equation and Scherrer formula derived from XRD patterns of CB and SB processed sample segments.

Sample ID	FWHM (degree) (112) peak	Crystallite size (nm) from Debye Scherer formula	Williamson – Hall analysis		
			Crystallite size (nm)	Types of strain	Strain (x 10^{-3})
SB1	0.2260	37.76	37.47	Tensile	3.17
SB2	0.2079	41.05	41.51	Tensile	3.55
SB3	0.1949	43.79	44.01	Tensile	3.27
SB4	0.1968	43.37	43.06	Tensile	2.78
CB1	0.1852	46.09	46.21	Tensile	2.19
CB2	0.170	50.21	51.35	Tensile	1.95
CB3	0.1680	50.80	50.05	Tensile	2.12
CB4	0.1676	50.93	50.60	Tensile	2.22

The X-ray diffraction (XRD) pattern of CIGS film selenized in SB and CB graphite box is shown in Fig. 2. The three major peaks corresponding to (112), (220) and (312) (JCPDS: 35-1102), confirming the chalcopyrite CIGS structure is present in all the segments, in agreement with the reported result [35]. Additional peaks corresponding to $MoSe_2$ (JCPDS: 29-0914) and Mo (JCPDS: 42-1102) also can be seen in the pattern. However, no peaks corresponding to the undesired secondary phases are observed. The preferred orientation peak intensity corresponding to the (112) plane becomes sharper in the CB sample than the SB sample, indicating an improvement in crystallinity.

The degree of enhancement of crystallinity of the film was studied by the full-width half maximum (FWHM) and the average crystallite size by

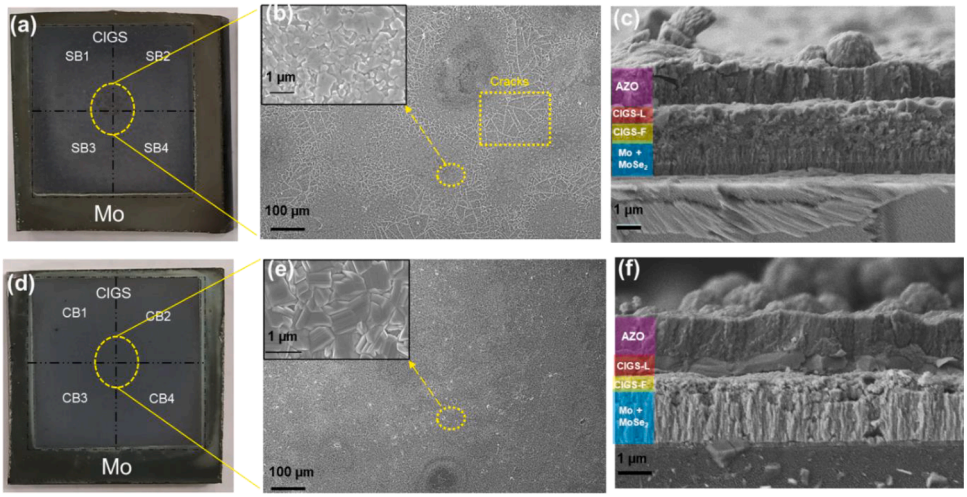

Fig. 3. Pictorial, surface FE-SEM and cross-sectional FESEM images of CIGS film selenized in SB (a, b, c) and CB (d, e, f), respectively. The insets in (b) and (e) show the corresponding FE-SEM image with higher magnification.

the Debye-Scherrer equation. The determined values of FWHM and average crystallite size for all SB and CB segments are listed in Table 2. The average crystallite size for all the four parts corresponding to SB exhibited lower values than its counterpart could be due to the non-homogeneous selenization resulting in improper selenization in the case of SB. Due to the rapid selenization in the RTP furnace, the strain may develop in both the films, which is determined by Williamsons-Hall (W-H) equation [36]:

$$\beta \cos\theta = \eta \sin\theta + \frac{\lambda}{B} \quad (1)$$

Where β is the FWHM of XRD peaks, θ is the Bragg diffraction angle, λ is the X-ray wavelength, B is the average crystallite size, and η is the strain. The strain in the film is determined from the plot between $\beta \cos\theta$ versus 4 * $\sin\theta$ for all the samples presented in the inset of the respective XRD spectrum.

The average crystallite size calculated from the W-H plot matches the Debye-Scherrer formula, as evident from Table 2. The strain calculated from the inset graph's slope reveals the tensile nature of the films, higher in the samples selenized in SB than CB. The lesser clearance volume of CB than SB gave rise to high Se vapor pressure resulting in lower strain and enhanced crystallite size; this logic is supported by the previously reported study [20].

In the XRD pattern of SB and CB processed CIGS films, a noticeable peak corresponding to the $MoSe_2$ phase can be seen, corresponding to the reaction of selenium vapor with the Mo film as selenium vapor infiltrates through the precursor film and reaches the Mo surface during the process. The selenization approach impacts quantitative $MoSe_2$ formation as it is directly related to the Se vapor distribution and pressure inside the graphite box. Earlier reports support the $MoSe_2$ formation at the Mo-CIGS interface; a thin layer of $MoSe_2$ enhances the adhesion and improves the Ohmic contact between CIGS and Mo [35].

Fig. 3 shows the pictorial image of CIGS films selenized in SB and CB and their corresponding surface and cross-sectional morphological FESEM images. From Fig. 3 (a) and (b), it is apparent that slight colour gradients are present from the center to the edge, suggesting non-homogeneous selenization and off-stichometry of the film. It is evident from Fig. 3 (b) that the film has multiple cracks marked in yellow color ascribed to high strain, whereas the magnified part exhibited varying grain size with voids as shown in the inset of Fig. 3 (b). It is anticipated that a considerable accumulation of Se vapor towards the SB corners due to the sharp edges may lead to the high SCIG ratio causing dark contrast in these regions compared to the center.

The cross-sectional morphology of CIGS film corresponding to the SB sample consists of a bi-layered structure, a CIGS-F layer of ~ 850 nm underneath a large crystalline grain of CIGS-L layer ~ 770 nm, as shown in Fig. 3 (c).

It is well reported that the bi-layered CIGS structure with a thin CIGS-L layer and thick CIGS-F layer increases the charge carrier recombination, which eventually leads to poor device performance [5]. Insufficient Se vapour supply at the bottom of the film promotes this kind of morphology and similar phenomena reported previously [17,37]. To realize large grains of the CIGS-L layer while minimizing the CIGS-F layer, CB was used instead of SB, maintaining other selenization conditions identical. This change immediately led to visibly better surface coverage with bigger grains, eliminating color gradients and cracks in the CIGS film, as shown in Fig. 3 (d) and (e). Circular and smooth corners of CB prevented the accumulation of Se vapor resulting in a non-gradient SCIG ratio and similar color contrast.

Moreover, it enhanced the grain size in a lateral direction, particularly of the CIGS-L layer minimizing the CIGS-F layer, as shown in Fig. 3 (f). This can be ascribed to maintaining uniform and adequate Se vapor pressure during the selenization process. It has been reiterated that the

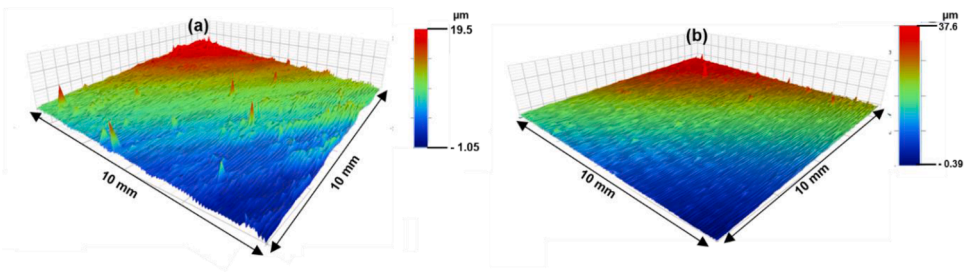

Fig. 4. Surface topography of selenized CIGS thin film in (a) SB, (b) CB.

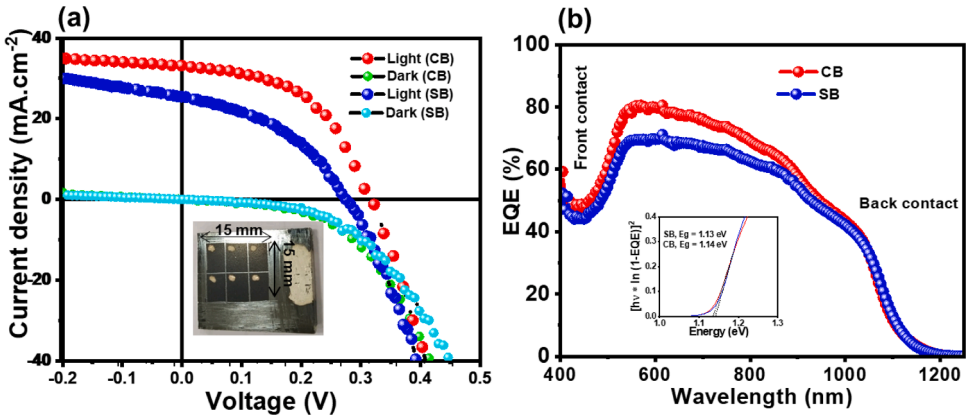

Fig. 5. (a) J-V characteristics and (b) EQE spectrum of CIGS solar cells prepared using absorber selenized in SB and CB (the inset is a plot of $[h\upsilon * \ln (1\text{-EQE})]^2$ against Energy (eV)).

Table 3
Photovoltaic parameters of best performed CIGS devices using SB and CB measured under AM1.5G illumination.

Sample ID	J_{sc} (mA/cm^2)	V_{oc} (mV)	FF (%)	η (%)	R_s (Ω. cm^2)	R_{sh} (Ω. cm^2)
SB	25.9	311	44.0	3.5	42.6	180.4
CB	32.0	320	49.0	5.2	28.1	478

round shape graphite box can potentially prevent the diffusion of Se vapor compare to the rectangular one, also supported by an earlier study discussed above. In contrast, large clearance volume and sharp corners in SB failed in providing constant Se vapor pressure over the area leading to rough and porous morphology.

The typical surface topography of the CIGS films selenized in CB and SB is studied by a 3D profilometer. A film area of 10 mm x 10 mm from the center was scanned, and corresponding surface characteristics are shown in Fig. 4. The CIGS film selenized in SB exhibits high irregularities compared to CB processed film. The surface is expected to provide an unfavorable condition for conformal coating or non-uniformity in thickness of the CdS layer, which subsequently defines the junction quality and solar cell device performance [38–40]. Whereas CB processed CIGS showed a smoother surface and well suited for conformal growth of CdS deposition.

Solar cells are fabricated using CIGS absorbers selenized in SB and CB. The current-voltage (J-V) characteristics under AM1.5G illumination is presented in Fig 5(a). As expected, the CIGS film prepared using the CB approach exhibited a higher power conversion efficiency of 5.2% on an active area of 0.18 cm^2 than that of the SB device. The photovoltaic parameters of the best cell out of six such as; open-circuit voltage (V_{oc}), short current density (J_{sc}), fill factor (FF), and power-conversion efficiency (η) obtained after the measurements are briefed in Table 3. Noticeable improvement in cell efficiency from 3.5% (SB) to 5.2% (CB) can be correlated to improved CIGS film quality in terms of grain size, smoothness, phase purity, and crystallinity of the absorber film. The cell processed in CB showed better V_{oc}, J_{sc}, and FF than the SB due to the suppression of the CIGS-F layer and reduced grain boundaries.

However, the complete elimination of this layer is required to improve the cell performance further as it provides high trap density states for the photo-generated charge carriers [5,22]. Moreover, the low V_{oc} and FF of the film can be attributed to the formation of thick $MoSe_2$ at the CIGS- Mo interface, which builds the potential barrier for effective charge carrier collection.

The external quantum efficiency (EQE) measurements of cells fabricated using the two graphite boxes are shown in Fig. 5 (b). The cell selenized in CB exhibited nearly 80% response in the wavelength region of 560 nm to 620 nm owing to better charge extraction and collection.

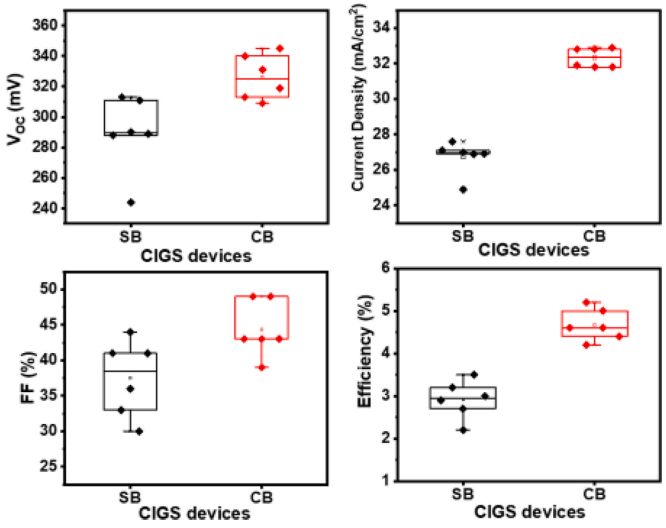

Fig. 6. Box plots of the J-V parameters of CIGS solar cells correspond to CB and SB.

The EQE response for SB was 70%, corresponding to the trap states in the bulk of the CIGS film. It is to be noted that the observed increase in EQE in the visible region in the case of CB processed CIGS film can be attributed to the significant increase in the collection of minority charge carriers.

The bandgap of absorber films determined by extrapolating the plots between $[h\upsilon * \ln(1\text{-EQE})]$ vs Energy (eV) that is estimated to be 1.13 eV and 1.14 eV for SB and CB processed CIGS films, respectively. The plots are shown in the inset of Fig. 5 (b). Typically, the V_{OC} of solar cell increases with an increasing bandgap of absorber film. In our case, the bandgap of CIGS films processed with CB and SB had not differed much, further confirmed from the Voc of fabricated solar cells. The gradual decay in the EQE response was observed after 620 nm in both cases. This behavior corresponds to the rear side recombination arising due to the presence of CIGS-F and thick $MoSe_2$. A slight decay below 560 nm is observed in all the cells, mainly due to the absorption in the n-type CdS layer.

The uniformity of selenization over the full printed area (15 mm × 15 mm) is further checked by the average device performance of the printed film. Six isolated cells on the total area are measured of each device corresponding to SB and CB. The resulting J-V parameters are represented as boxplots in Fig. 6. Each device is isolated by mechanical scribing, as shown in the inset of Fig. 5 (a). It is evident from the results that the average efficiency of six cells corresponding to CB is higher than

Table 4
Summary of performance characteristics and other relevant parameters for CIGS thin film solar cells prepared by inkjet printing and non-vacuum based method.

Absorber	Precursor/ Technique	PCE(%)	V_{OC}(mV)	J_{sc}(mA/ cm^2)	FF (%)	R_s(Ω. cm^2)	R_{sh}(Ω. cm^2)	Pre-treatment	Selenization	Post-selenization	Ref.
CIGS	Metal acetate, IPA, **Inkjet printing**	5.04 (A=0.04 cm^2)	386	29.8	44	5.28	95.9	300 °C for few minutes	500 °C/20 min (Se powder/ H_2/ N_2) in a quartz tube furnace)	None	Wang et. al. 2006 [42]
CIGSSe	Metal nitrates, IPA, **Inkjet printing**	11.3 (A= 0.5 cm^2)	541	31.1	67	NA	NA	250 °C for few minutes	400 °C/22 min/560 °C/ 22 min/580 °C/ 10 min (Se+Ar/ Ar+Se+H_2S)	Use of $(NH_4)_2S$ and KCN	Lin et al. 2015 [5]
CIGSSe	Cu_2S,In_2Se_3,Ga, Se,S, N_2H_4 **Spin coating**	17.3 (A = 0.45 cm^2)	660	35.7	73	0.8	735	340 °C for 5 min	500-600 °C (Ga grading)	None	Zang et. al. 2016 [4]
CIGS	Metal nitrates, DI water, **Inkjet printing**	5.2 (A= 0.16 cm^2)	320	33	49	28	478	150 °C for 1 min	250 °C/10 min/550 °C/ 14 min (Se pellets +N_2)	None	This work

its counterpart.

Moreover, other photovoltaic parameters such as J_{sc}, V_{oc}, and FF are higher than the sample selenized in SB. However, the V_{oc} of both the CIGS devices is relatively lower than the state-of-the-art device [41] due to the untraceable conducting defects such as $Cu_{2-X}Se_X$ in the absorber layer, ineffective absorption to CIGS-F layer and recombination assisted by the thick $MoSe_2$ layer.

To put our findings in context, the comparative photovoltaic performance of best reported precursor-based CIGS thin film solar cells by non-vacuum route, solar cells by inkjet printing along with the findings from the present work summarized in Table 4.

Compare to state of the art, non-vacuum-based CIGS device, which shows $J_{sc} > 33$ mA/cm^2, the current density measured from our device is close to this value and more than the other inkjet printed reports, correspond to efficient collection of ~ 80% of the photons above or equal to the bandgap by a printed CIGS absorber film. Hence, the current density of our printed device is promising. However, our fabricated CIGS device suffered from significant V_{oc} and FF limitations compared to other mentioned reports in Table 4. Nevertheless, uniform and optimum selenium vapor pressure are required to minimize the fine-grained layer and $MoSe_2$ layer, which can be achieved by various means such as a depositing thin barrier layer on top of Mo film, and multiple selenization steps, etc. There has a great potential to improve our CIGS device performance by optimizing the process parameter more precisely. We have demonstrated a reasonable PCE of 5.2% on the active area of 0.16 cm^2 employing a circular graphite box.

4. Conclusions

A comparative investigation on the effect of Se vapor distribution using two different geometries of boxes is presented. The inkjet printed CIG film selenized in SB exhibited off-stoichiometry, non-uniform grains, color gradient and cracks on the surface attributed to inadequate and non-constant Se vapor distribution originated by the geometrical constraint of the box. The redesigned features of CB, such as smooth side corners and lower clearance volume, helped in maintaining the Se vapor distribution uniformly and adequately throughout the selenization. This leads to high-quality CIGS formation with high crystallinity, a very thin CIGS-F layer and larger grains on the surface and along the cross-section. The device fabricated using CB demonstrated 5.2% efficiency, which is higher than that of the using SB. However, incomplete elimination of CIGS-F layer and thick $MoSe_2$ at CIGS- Mo interface induces gradual decay of the EQE curve after 620 nm suggesting that the selenization process could be further fine-tuned to reduce the back-contact recombination.

Declaration of Competing Interest

The authors declare that they have no known competing financial interests or personal relationships that could have appeared to influence the work reported in this paper.

Acknowledgements

This work is supported by ARCI-Technology Research Center (TRC) {Ref. No. Al/1/65/ARCI/2014(c)} through Department of Science and Technology (DST), India. The authors are thankful to Director ARCI for permitting us to publish this work. We thank Dr K. Suresh (CMCT, ARCI) and Dr Sreekanth Mandati (CSEM, ARCI) to support the characterization of CIGS thin films. We also would like to thank Ms Ramya Krishna Battula (CSEM, ARCI) for performing the EQE measurements of CIGS solar cells.

References

[1] M. Nakamura, K. Yamaguchi, Y. Kimoto, Y. Yasaki, T. Kato, H. Sugimoto, Cd-free Cu(In,Ga)(Se,S) 2 thin-film solar cell with record efficiency of 23.35%, IEEE J. Photovoltaics. 9 (2019) 1863–1867, https://doi.org/10.1109/JPHOTOV.2019.2937218.
[2] A. Chirilă, S. Buecheler, F. Pianezzi, P. Bloesch, C. Gretener, A.R. Uhl, C. Fella, L. Kranz, J. Perrenoud, S. Seyrling, R. Verma, S. Nishiwaki, Y.E. Romanyuk, G. Bilger, A.N. Tiwari, Highly efficient Cu(In,Ga)Se2 solar cells grown on flexible polymer films, Nat. Mater. 10 (2011) 857–861, https://doi.org/10.1038/nmat3122.
[3] T.K. Todorov, O. Gunawan, T. Gokmen, D.B. Mitzi, Solution-processed Cu(In,Ga)(S, Se) 2 absorber yielding a 15.2% efficient solar cell, Prog. Photovoltaics Res. Appl. 21 (2013) 82–87, https://doi.org/10.1002/pip.1253.
[4] T. Zhang, Y. Yang, D. Liu, S.C. Tse, W. Cao, Z. Feng, S. Chen, L. Qian, High efficiency solution-processed thin-film Cu(In,Ga)(Se,S) 2 solar cells, Energy Environ. Sci. 9 (2016) 3674–3681, https://doi.org/10.1039/C6EE02352E.
[5] X Lin, R Klenk, L Wang, T Köhler, J Albert, S Fiechter, A Ennaoui, M.C Lux-Steiner, 11.3% efficiency Cu(In,Ga)(S,Se) 2 thin film solar cells via drop-on-demand inkjet printing, Energy Environ. Sci. 9 (2016) 2037–2043, https://doi.org/10.1039/C6EE00587J.
[6] G.S. Park, V.Ben Chu, B.W. Kim, D.-W. Kim, H.-S. Oh, Y.J. Hwang, B.K. Min, Achieving 14.4% alcohol-based solution-processed Cu(In,Ga)(S,Se) 2 thin film solar cell through interface engineering, ACS Appl. Mater. Interfaces 10 (2018) 9894–9899, https://doi.org/10.1021/acsami.8b00526.
[7] U. Berner, M. Widenmeyer, Solution-based processing of Cu(In,Ga)Se 2 absorber layers for 11% efficiency solar cells via a metallic intermediate, Prog. Photovoltaics Res. Appl. 23 (2015) 1260–1266, https://doi.org/10.1002/pip.2546.
[8] S. Wu, J. Jiang, S. Yu, Y. Gong, W. Yan, H. Xin, W. Huang, Over 12% efficient low-bandgap CuIn(S, Se)2 solar cells with the absorber processed from aqueous metal complexes solution in air, Nano Energy 62 (2019) 818–822, https://doi.org/10.1016/j.nanoen.2019.06.010.
[9] A.R. Uhl, J.K. Katahara, H.W. Hillhouse, Molecular-ink route to 13.0% efficient low-bandgap CuIn(S,Se) 2 and 14.7% efficient Cu(In,Ga)(S,Se) 2 solar cells, Energy Environ. Sci. 9 (2016) 130–134, https://doi.org/10.1039/C5EE02870A.
[10] S.R. Dhage, B.S. Yadav, G.K. Jha, A.C. Badgujar, 12.95% Efficient Cu(In,Ga)Se 2 solar cells by single-step atmospheric selenization, scaled to monolithically

integrated modules, ACS Appl. Energy Mater. 4 (2021) 286–294, https://doi.org/10.1021/acsaem.0c02254.
[11] D. Lee, K. Yong, Non-vacuum deposition of CIGS absorber films for low-cost thin film solar cells, Korean J. Chem. Eng. 30 (2013) 1347–1358, https://doi.org/10.1007/s11814-013-0101-0.
[12] M. Park, S. Ahn, J.H. Yun, J. Gwak, A. Cho, S. Ahn, K. Shin, D. Nam, H. Cheong, K. Yoon, Characteristics of Cu(In,Ga)Se2 (CIGS) thin films deposited by a direct solution coating process, J. Alloys Compd. 513 (2012) 68–74, https://doi.org/10.1016/j.jallcom.2011.09.080.
[13] S.J. Park, E. Lee, H.S. Jeon, S.J. Ahn, M.-K. Oh, B.K. Min, A comparative study of solution based CIGS thin film growth on different glass substrates, Appl. Surf. Sci. 258 (2011) 120–125, https://doi.org/10.1016/j.apsusc.2011.08.016.
[14] S. Ahn, C. Kim, J.H. Yun, J. Gwak, S. Jeong, B.-H. Ryu, K. Yoon, CuInSe 2 (CIS) thin film solar cells by direct coating and selenization of solution precursors, J. Phys. Chem. C 114 (2010) 8108–8113, https://doi.org/10.1021/jp1007363.
[15] O. Lundberg, M. Edoff, L. Stolt, The effect of Ga-grading in CIGS thin film solar cells, Thin Solid Films (2005) 520–525, https://doi.org/10.1016/j.tsf.2004.11.080, 480–481.
[16] J. Bi, J. Ao, M.-J. Jeng, L. Yao, S. Gao, G. Sun, Q. He, Z. Zhou, Y. Sun, Y.-L. Xiao, L.-B. Chang, Three-step vapor Se/N_2/vapor Se reaction of electrodeposited Cu/In/Ga precursor for preparing $CuInGaSe_2$ thin films, Sol. Energy Mater. Sol. Cells 159 (2017) 352–361, https://doi.org/10.1016/j.solmat.2016.09.026.
[17] L. Zhang, D. Zhuang, M. Zhao, Q. Gong, L. Guo, L. Ouyang, R. Sun, Y. Wei, S. Zhan, The effects of selenium content on Cu(InGa)Se_2 thin film solar cells by sputtering from quaternary target with Se-free post annealing, Vacuum 137 (2017) 205–208, https://doi.org/10.1016/j.vacuum.2016.12.041.
[18] Chia-Hao Hsu, Wei-Hao Ho, Chih-Huang Lai, Effects of Se flux on the properties of the quaternary-sputtered CIGS thin film solar cells. in: 2015 IEEE 42nd Photovolt. Spec. Conf., IEEE, 2015, pp. 1–4, https://doi.org/10.1109/PVSC.2015.7356094.
[19] A.E. Zaghi, M. Buffière, G. Brammertz, N. Lenaers, M. Meuris, J. Poortmans, J. Vleugels, Selenization of printed Cu–In–Se alloy nanopowder layers for fabrication of CuInSe 2 thin film solar cells, Thin Solid Films 582 (2015) 18–22, https://doi.org/10.1016/j.tsf.2014.10.038.
[20] J.H. Han, S. Rehan, D.G. Moon, A. Cho, J. Gwak, K.H. Yoon, S.K. Ahn, J.H. Yun, Y. J. Eo, S. Ahn, Actual partial pressure of Se vapor in a closed selenization system: quantitative estimation and impact on solution-processed chalcogenide thin-film solar cells, J. Mater. Chem. A 4 (2016) 6319–6331, https://doi.org/10.1039/C6TA00145A.
[21] Soňa Uličná, Solution-Processing of Cu(In,Ga)(S,Se)2 Solar Cells From Metal Chalcogenides – Aspects of Absorber Crystallization and Interface Formation, Loughborough University, 2019.
[22] D. Zhao, Q. Fan, Q. Tian, Z. Zhou, Y. Meng, D. Kou, W. Zhou, S. Wu, Eliminating fine-grained layers in Cu(In,Ga)(S,Se) 2 thin films for solution-processed high efficiency solar cells, J. Mater. Chem. A 4 (2016) 13476–13481, https://doi.org/10.1039/C6TA05728D.
[23] Jonathan James Scragg, Studies of Cu_2ZnSnS_4 Films Prepared by Sulfurization of Electrodeposited Precursors, University of Bath, 2010.
[24] A.C. Badgujar, S.R. Dhage, S.V. Joshi, Process parameter impact on properties of sputtered large-area Mo bilayers for CIGS thin film solar cell applications, Thin Solid Films 589 (2015) 79–84, https://doi.org/10.1016/j.tsf.2015.04.046.
[25] B.S. Yadav, A.C. Badgujar, S.R. Dhage, Effect of various surface treatments on adhesion strength of magnetron sputtered bi-layer Molybdenum thin films on soda lime glass substrate, Sol. Energy 157 (2017) 507–513, https://doi.org/10.1016/j.solener.2017.08.068.
[26] B.S. Yadav, S.R. Dey, S.R. Dhage, Effective ink-jet printing of aqueous ink for Cu (In, Ga) Se_2 thin film absorber for solar cell application, Sol. Energy 179 (2019) 363–370, https://doi.org/10.1016/j.solener.2019.01.003.
[27] B.S. Yadav, S.Ranjan Day, S.R. Dhage, Chalcopyrite CIGS absorber layer by inkjet printing for photovoltaic application, Mater. Today Proc. 4 (2017) 12480–12483, https://doi.org/10.1016/j.matpr.2017.10.047.
[28] V Haug, Cu(In,Ga)Se_2 thin-film solar cells based on a simple sputtered alloy precursor and a low-cost selenization step, J. Photonics Energy. 1 (2011), 018002, https://doi.org/10.1117/1.3659500.
[29] S. Zweigart, S. Sun, G. Bilger, H. Schock, CuInSe 2 film growth using precursors deposited at low temperature, Sol. Energy Mater. Sol. Cells (1996) 219–229, https://doi.org/10.1016/0927-0248(95)00101-8, 41–42.
[30] V. Gremenok, E. Zaretskaya, V. Zalesski, K. Bente, W. Schmitz, R. Martin, H. Moller, Preparation of Cu(In,Ga)Se_2 thin film solar cells by two-stage selenization processes using N_2 gas, Sol. Energy Mater. Sol. Cells 89 (2005) 129–137, https://doi.org/10.1016/j.solmat.2004.11.014.
[31] B.S. Yadav, S. Koppoju, S.R. Dey, S.R. Dhage, Microstructural investigation of inkjet printed Cu(In,Ga)Se<inf>2</inf>thin film solar cell with improved efficiency, J. Alloys Compd. 827 (2020), https://doi.org/10.1016/j.jallcom.2020.154295.
[32] P. Uday Bhaskarand, S.R. Dhage, CdSBuffer layer by CBD on 300 mm × 300 mm Glass for CIGS Solar Cell Application, Mater. Today Proc. 4 (2017) 12525–12528, https://doi.org/10.1016/j.matpr.2017.10.055.
[33] S.R. Dhage, A.C. Badgujar, Transparent conducting Al:ZnO thin films on large area by efficient cylindrical rotating DC magnetron sputtering, J. Alloys Compd. 763 (2018) 504–511, https://doi.org/10.1016/j.jallcom.2018.05.234.
[34] G. Li, W. Liu, Y. Liu, S. Lin, Y. Zhang, Z. Zhou, Q. He, Y. Sun, The influence of cracked selenium flux on CIGS thin film growth and device performance prepared by two-step selenization processes, Sol. Energy Mater. Sol. Cells 139 (2015) 108–114, https://doi.org/10.1016/j.solmat.2015.03.021.
[35] T. Wada, N. Kohara, T. Negami, M. Nishitani, Chemical and structural characterization of $\bf Cu(In,Ga)Se_{2}/Mo$ interface in $\bf Cu(In,Ga)Se_{2}$ solar cells, Jpn. J. Appl. Phys. 35 (1996) L1253–L1256, https://doi.org/10.1143/JJAP.35.L1253.
[36] A.B. Rohom, P.U. Londhe, N.B. Chaure, Rapid thermal processed CuInSe 2 layers prepared by electrochemical route for photovoltaic applications, J. Electrochem. Soc. 165 (2018) H3051–H3060, https://doi.org/10.1149/2.0081804jes.
[37] H. Young Park, D. Gwon Moon, J. Ho Yun, S.K. Ahn, K.H. Yoon, S. Ahn, Efficiency limiting factors in Cu(In,Ga)Se 2 thin film solar cells prepared by Se-free rapid thermal annealing of sputter-deposited Cu-In-Ga-Se precursors, Appl. Phys. Lett. 103 (2013), 263903, https://doi.org/10.1063/1.4852597.
[38] V. Garg, B.S. Sengar, P. Sharma, A. Kumar, S.Kumar Aaryashree, S. Mukherjee, Sputter-instigated plasmon-enhanced optical backscattering layer in ultrathin solar cells: Application of GZO in CIGSe material system, Sol. Energy 174 (2018) 35–44, https://doi.org/10.1016/j.solener.2018.08.074.
[39] V. Garg, B.S. Sengar, A. Kumar, G. Siddharth, S. Kumar, S. Mukherjee, Investigation of valence plasmon excitations in GMZO thin film and their suitability for plasmon-enhanced buffer-less solar cells, Sol. Energy 178 (2019) 114–124, https://doi.org/10.1016/j.solener.2018.12.017.
[40] Z. Jehl, M. Bouttemy, D. Lincot, J.F. Guillemoles, I. Gerard, A. Etcheberry, G. Voorwinden, M. Powalla, N. Naghavi, Insights on the influence of surface roughness on photovoltaic properties of state of the art copper indium gallium diselenide thin films solar cells, J. Appl. Phys. 111 (2012), 114509, https://doi.org/10.1063/1.4721648.
[41] P. Jackson, D. Hariskos, R. Wuerz, O. Kiowski, A. Bauer, T.M. Friedlmeier, M. Powalla, Properties of Cu(In,Ga)Se 2 solar cells with new record efficiencies up to 21.7%, Phys, Status Solidi - Rapid Res. Lett 9 (2015) 28–31, https://doi.org/10.1002/pssr.201409520.
[42] W. Wang, Y.-W. Su, C. Chang, Inkjet printed chalcopyrite CuInxGa1−xSe_2 thin film solar cells, Sol. Energy Mater. Sol. Cells 95 (2011) 2616–2620, https://doi.org/10.1016/j.solmat.2011.05.011.